ADVANCED FUNCTIONAL MATERIALS
www.afm-journal.de

# Topography-Supported Nanoarchitectonics of Hybrid Scaffold for Systematically Modulated Bone Regeneration and Remodeling

*Tae-Sik Jang, Seong Je Park, Ji Eun Lee, Jeongho Yang, Suk-Hee Park, Martin Byung-Guk Jun, Young Won Kim, Clodualdo Aranas, Joon Phil Choi, Yu Zou, Rigoberto C. Advincula, Yufeng Zheng, Hae Lin Jang, Nam-Joon Cho, Hyun-Do Jung,* and Sang Hoon Kim**

**Orthopedic implants should have sufficient strength and promote bone tissue regeneration. However, most conventional implants are optimized for use either under high mechanical load or for active osseointegration. To achieve the dual target of mechanical durability and biocompatibility, polyether ether ketone (PEEK) filaments reinforced with internal titanium dioxide ($TiO_2$) nanoparticles via dopamine-induced polymerization are additively manufactured into an orthopedic implant through material extrusion (ME). The exterior of the PEEK/$TiO_2$ composite is coated with hydroxyapatite (HA) using radiofrequency (RF) magnetron sputtering to increase both the strength and biocompatibility provided by homogeneous ceramic–ceramic interactions and the protuberant nanoscale topography between the internal $TiO_2$ nanoparticle reinforcement and external HA coating. The hardness, tensile, and compression, and scratch test results demonstrate a considerable enhancement in the mechanical strength of the hierarchical PEEK/TiO2/HA hybrid composite structure compared to that of the conventional 3D-printed PEEK. Furthermore, PEEK with internal $TiO_2$ reinforcement improves the proliferation and differentiation of bone cells in vitro, whereas the external HA coating leads to a more prevalent osteoblast absorption. Micro-computed tomography and histological analyses confirm new bone formation and a high bone-to-implant contact ratio on the HA-coated PEEK structure reinforced with $TiO_2$ nanoparticles.**

## 1. Introduction

With the aging of modern population and frequent occurrence of fracture accidents, the development of a smart implant with a sufficient strength benefit and high bone tissue regeneration capability has shown a remarkable potential to revolutionize the healthcare system.[1–3] Compared with natural bone, which depending on the type, has a relatively wide elastic modulus range of 3–30 GPa, an artificial bone implant composed of polyether ether ketone (PEEK) has a significantly narrower elastic modulus range of 3–4 GPa.[4–6] Even so, it would be more useful to control the mechanical strength of the PEEK implant over a wider range to increase its similarity to natural bone.[7,8] However, PEEK demonstrates bioinertness, inferior cell adhesion and growth, and poor integration with the surrounding bone.[9,10] A high percentage of post-orthopedic implant surgery failures are caused by the disintegration of PEEK implant with natural bone at the contact site (interface) with

T.-S. Jang
Department of Materials Science and Engineering
Chosun University
Gwangju 61452, Republic of Korea
S. J. Park
Department of Mechanical Design Engineering
Hanyang University
Seoul 04763, Republic of Korea

The ORCID identification number(s) for the author(s) of this article can be found under https://doi.org/10.1002/adfm.202206863.



**DOI: 10.1002/adfm.202206863**

S. J. Park, S. H. Kim
Advanced Joining and Additive Manufacturing R&D Department
Korea Institute of Industrial Technology
Siheung, Gyeonggi-do 15014, Republic of Korea
E-mail: sanghooni791@kitech.re.kr
J. E. Lee
Advanced Textile R&D Department
Korea Institute of Industrial Technology
Ansan, Gyeonggi-do 15588, Republic of Korea
J. Yang, S.-H. Park
School of Mechanical Engineering
Pusan National University
Busan 46241, Republic of Korea
M. B.-G. Jun, Y. W. Kim
School of Mechanical Engineering
Purdue University
West Lafayette, IN 47907, USA

 

natural bone, which requires additional surgeries.[11] Therefore, surface engineering of PEEK could be an effective roadmap for enhancing its biocompatibility with natural bone.[9,12] Various secondary constituents, such as synthetic polymers, glass particles, bioactive inorganics, and ceramic resins (**Table 1**), are incorporated by direct reinforcement, surface coating, and uniform blending with the primary PEEK scaffolds in order to enhance both the mechanical strength and bone tissue regeneration capacity; among previous results, the incorporation of Ti-based materials into PEEK implants has positive effects in bone scaffolds, accelerating the rates of osteoblast adhesion, proliferation, and differentiation.[12,13] Previously, we determined the bone regeneration capability of Ti-coated PEEK implants 12 weeks after implantation in a rabbit tibia defect model.[14] Despite the enhanced mechanical strength of Ti-based alloys, there are two key drawbacks to Ti-based alloys when used as bioimplant reinforcement: Ti exfoliation on the surface of the composite prosthesis in contact with natural bone, which results in the production of toxic $Ti_2$+ via erosion and corrosion due to cellular activity, and the release of these toxins into body fluids.[10,15–17] First, due to the heterogeneous metal-organic conjugation between Ti and PEEK in the composite prosthesis in contact with natural bone, Ti can be exfoliated, which can cause poor integration with cells and tissues after implantation.[18] Second, Ti in the physiological environment is converted into toxic soluble $Ti_2$+ that can spread throughout the body, impair metabolic functions, and promote DNA damage.[19,20] In contrast to the adverse effects of Ti, stable titanium dioxide ($TiO_2$) increases the abrasion resistance of implants against external pressure and force and is also physiologically inert. For example, as well as being resistant to acid dissolution, enzymatic redox reactions, and mineral-based catalysis, $TiO_2$-sputtered PEEK implants exhibit high osteogenic differentiation (for example, both the proliferation and differentiation of mesenchymal stem cells were promoted simultaneously) and low neutrophil and macrophage infiltration, which is indicative of low postoperative inflammation.[21,22] In addition, the biocompatibility of hydroxyapatite (HA) in mammals has been extensively studied. For example, previous studies reported that an HA implant promoted osteoblastic cell proliferation and facilitated the expression of bone-specific proteins, including type I collagen.[23,24] However, HA is more useful as a coating material for load-bearing orthopedic implants than as a structural substance itself, because it is a brittle ceramic and, thus, has relatively low strain and fracture resistance.[23,24] Hence, reinforcing and coating PEEK with $TiO_2$ and HA, respectively, allows for the development of more advanced orthopedic implants.

In this study, we explain how and why PEEK can be internally reinforced with $TiO_2$ using dopamine-induced polymerization and material extrusion (ME), followed by external coating with HA using radiofrequency (RF) magnetron sputtering to improve the mechanical strength (hardness, tensile and compressive strength, and scratch resistance) of the resulting hybrid composite compared with conventional PEEK (**Scheme 1**). It has been determined that embedding $TiO_2$ nanoparticles into PEEK creates a nanoscale rough adlayer via migration toward areas with less shear force, which is consistent with the suspension balance model. Subsequently, the HA layer formed homogeneous ceramic-ceramic interactions with $TiO_2$ nanoparticles (producing higher mechanical strength and scratch resistance), in contrast to heterogeneous ceramic-polymer interactions between $TiO_2$ nanoparticles and PEEK, in which the HA coating was more tightly bound to the $TiO_2$ nanoparticles embedded on PEEK than it was directly coated onto PEEK. We also evaluated the preosteoblast cellular responses (cell adhesion, proliferation, and osteoblastic differentiation) to bioactive composites with and without the HA coating. Furthermore, the additively manufactured orthopedic scaffolds were implanted into rabbits with femoral defects. The osteogenic and osseointegration properties of the additively manufactured scaffolds were compared with those of a conventional

C. Aranas
Department of Mechanical Engineering
University of New Brunswick
Fredericton, New Brunswick E3B 5A3, Canada
J. P. Choi
Department of 3D Printing
Korea Institute of Machinery & Materials
Daejeon 34103, Republic of Korea
Y. Zou
Department of Materials Science and Engineering
University of Toronto
Toronto, Ontario M5S 3E4, Canada
R. C. Advincula
Department of Macromolecular Science and Engineering
Case Western Reserve University
Cleveland, OH 44106, USA
R. C. Advincula
Department of Chemical and Biomolecular Engineering and
Joint Institute for Advanced Materials
University of Tennessee
Knoxville, TN 37996, USA
R. C. Advincula
Center for Nanophase Materials and Sciences
Oak Ridge National Laboratory
Oak Ridge, TN 37830, USA
Y. Zheng
School of Materials Science and Engineering
Peking University
Beijing 100871, China
H. L. Jang
Center for Engineered Therapeutics
Department of Medicine and Orthopedic Surgery
Brigham and Women's Hospital
Harvard Medical School
Boston, MA 02115, USA
N.-J. Cho
School of Materials Science and Engineering
Nanyang Technological University
Singapore 637553, Singapore
H.-D. Jung
Department of Biotechnology
The Catholic University of Korea
Bucheon, Gyeonggi-do 14662, Republic of Korea
E-mail: hdjung@catholic.ac.kr
H.-D. Jung
Department of Biomedical and Chemical Engineering (BMCE)
The Catholic University of Korea
Bucheon, Gyeonggi-do 14662, Republic of Korea

**Table 1.** Comparison of Additively Manufactured Composite Orthopedic Implants.

| Fabrication utilized | Matrix material | Reinforcement material | Surface morphology | Mechanical testing | Improved strength | In vitro model | In vivo odel | Reference |
|---|---|---|---|---|---|---|---|---|
| Blending and casting | Polyether ether ketone/poly (ether imide) blends | $TiO_2$ nanoparticles | Smooth surface | Water-absorption, tensile, and tribological properties | Elastic modulus increased from 3.9 to 5.7 GPa | Under UV illumination, *Escherichia coli* activity was hindered with 4.0 wt.% $TiO_2$ nanoparticles | – | [25] |
| Machined | Polyether ether ketone | $Ta_2O_5$ nanoparticles | Protuberant surface | Nanoindentation | Elastic modulus increased from 5.5 to 9.5 GPa after reinforcement | Cell culturing of rat bone mesenchymal stem cells | A rat femur model | [26] |
| Pressed | Poly-D,L-lactide-glycolide | $\beta$-calcium silicate | Porous structure | Compressive strength and toughness | Porosity of 70.9 ± 0.9% and compressive strength of 5.01 ± 0.35 MPa | Rat bone marrow-derived stem cells and human umbilical vein endothelial cells | Implanted in rabbit femur defects (6 × 10 mm) with $\beta$-tricalcium phosphate (rabbit femur defect model) | [27] |
| Hydrogel synthesis | Photocrosslinkable gelatin methacryloyl | PEG-dopamine-Fe-based magnetic nanoparticles | A porous and interconnected network | Compressive strength | Elastic modulus increased to 26.7 ± 4.7 kPa | Human bone marrow stem cells and murine-derived preosteoblasts | – | [28] |
| Hot-melt extrusion | Polycaprolactone or poly(lactic-co-glycolic acid) | HA | Porous and a fine web-like network structure | Cyclic axial compression and recovery | Strain-to-failure increased from 32% to 67% and elastic modulus from 4 to 11 MPa with 50% porosity | Bone marrow-derived human mesenchymal stem cells cultured in vitro over 4 weeks | A mouse subcutaneous implant model, a rat posterolateral spinal fusion model, and a primate calvarial defect model | [29] |
| Electrospinning | Poly(lactide-co-glycolide)-b-poly(ethylene glycol)-b-poly(lactide-co-glycolide) | HA | Isotropically distributed fiber meshes | Stress-controlled cyclic thermal-mechanical testing | Tensile strength of 0.3 MPa and tensile strain of 25% after full shape recovery at 50°C | Green fluorescent protein-labeled rat bone marrow-derived stromal cells | – | [30] |
| Extruding, spreading, and leaching | Citrate/phosphoserine biodegradable polymer | NaCl and HA | Porous after NaCl leaching | Compressive strength | Compressive strength of 200 MPa | Human mesenchymal stem cells | Rat femoral-condyle and cranial defect models | [31] |
| Gelification | Bisphosphonate-functionalized gelatin | Bioactive glass particles | Rough surface | Storage modulus with self-healing ability | Elastic modulus of 10 MPa according to the reinforcement ratio | Cell proliferation and differentiation of osteoblast precursor cells | An osteoporotic rat bone defect model | [32] |
| Spray-coated on a Co–Cr stent | Biodegradable poly(lactide-co-glycolide) | Modified magnesium hydroxide nanoparticles | Rough surface | Tensile testing | Tensile strength increased from 4 to 12 MPa | Human hematopoietic cells and human umbilical vein endothelial cells (increased cell viability) | A rat subcutaneous model, intracoronary stenting in a porcine model, and a mouse partial nephrectomy model | [33] |

## 2. Results and Discussion

### 2.1. Grafting (Immobilizing) of $TiO_2$ Nanoparticles on PEEK Filaments

Various complex redox processes and a series of intermediates (**Figure 1**a) were induced by covalent polymerization of dopamine and non-covalent self-assembly with $Ti^{4+}$. Dopamine was converted to quinone before undergoing further oxidation and intramolecular cyclization to form 5,6-dihydroxyindole (DHI).[34] In addition to DHI dimerization, partial peroxidative fission of *o*-quinone also occurred as a result of the formation of various catecholamine-based oligomer quinone species.[34] This is contrary to the findings of Marco et al., who reported that synthesized polydopamine consisted mainly of DHI-derived units.[34] In this respect, the utilization of the polydopamine conjugated with the $Ti^{4+}$ can result in the uniform dispersion and further tight adhesion of the Ti precursor ions on the surface of the polyether ether ketone (PEEK) filament immediately before the material extrusion (ME).[35,36] In particular, since PEEK has high thermal and chemical stability, polydopamine was applied as the intermediate adhesive for the interfacial bonding between the organic (PEEK polymer) and inorganic (the Ti ions turned into the $TiO_2$ nanoparticles later). With the similar reason, the

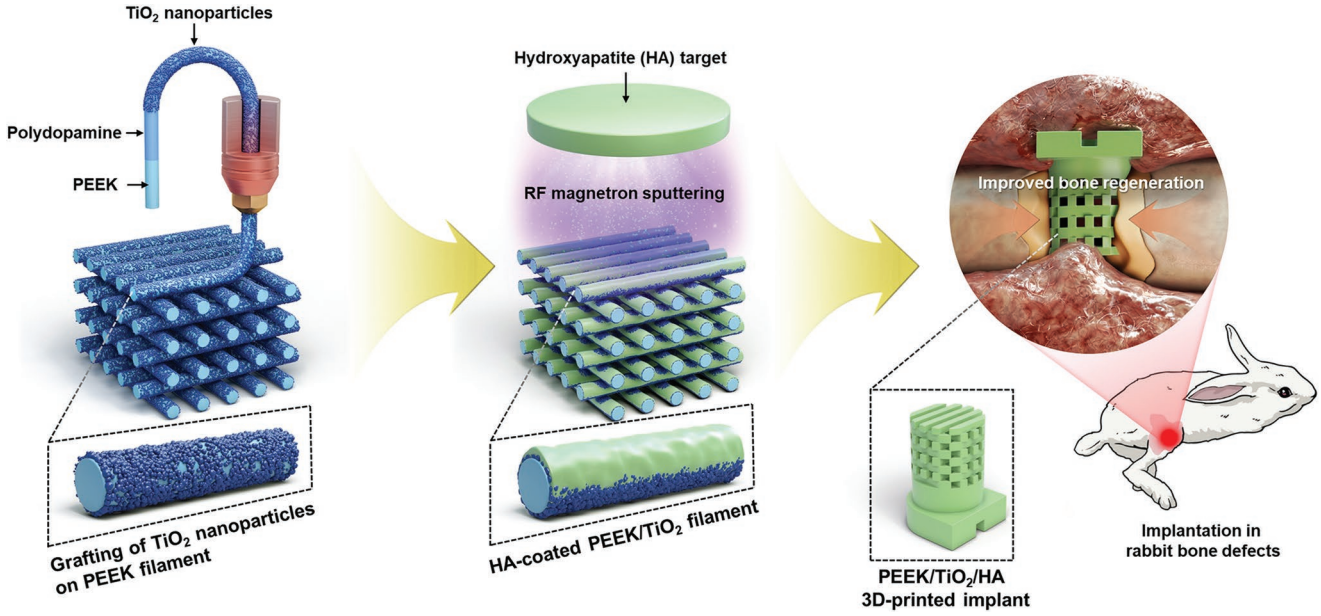


**Scheme 1.** Schematic of fabrication procedure of a PEEK/$TiO_2$/HA 3D-printed implant along with in vivo scaffold implantation in a rabbit.

direct application of the $TiO_2$ nanoparticles as the precursor was avoided owing to their high agglomeration tendency and frictional damaging and blocking on the heating nozzle. Thereafter, thermal diffusion through the heated nozzle during ME degraded all of the cross-linked (bio-conjugated) polydopamine derivatives, unreacted dopamine, and impurities, leaving only $TiO_2$ nanoparticles on the PEEK surface. In fact, when the substrate was coated with polydopamine, it was determined in general that its thermal stability maintained up to the temperature of 227 °C.[37,38] Above 227 °C, however, two significant thermal degradations occurred during temperature ranges from 227 to 300 °C and from 300 to 400 °C: the first degradation was consistent with the degradation of the catechol moieties, whereas the second degradation was most likely due to the decomposition of the pyrrole and indole groups, leading to the degradation of the whole polydopamine molecules.[37,38] The remaining $TiO_2$ nanoparticles, which were unaffected, tightly adhered on the adlayer of the as-printed PEEK substance. The surface morphologies of PEEK filaments covered with three different amounts (0.00, 1.78, or 4.48 wt.%) of $TiO_2$ nanoparticles are compared in Table S1 (Supporting Information) and Figure 1. The surface of the pristine PEEK filaments in Figure 1b was relatively smooth, although some irregular fragments of several hundred nanometers in size caused by hot extrusion of precursor PEEK pieces and their agglomeration were observed on the surface. Thus, the elemental mapping images in Figure S1 (Supporting Information) show that C and O elements were the main chemical constituents of untreated PEEK filaments. Moreover, Figure 1c shows that $TiO_2$ nanoparticles were uniformly anchored to the uppermost surface of the $TiO_2$ nanoparticle-treated PEEK filaments. The immobilization of more $TiO_2$ nanoparticles according to their concentration during formation of the polydopamine adhesive caused the PEEK filaments to be more densely covered by a higher fraction of $TiO_2$ nanoparticles before the additive manufacturing process (Figure 1d). Meanwhile, Ti, C, and O elements were present on the surface of the PEEK filaments, as shown in Figure 1e.

### 2.2. Migration Mechanism of $TiO_2$ Nanoparticles to Produce an Adlayer of PEEK and an HA Coating on the PEEK/$TiO_2$ Composite

During ME, PEEK fluid melted using a heated nozzle provided an effective diffusion environment in which the $TiO_2$ nanoparticles migrated readily into the PEEK polymer. Therefore, although ceramic nanoparticles were present on the surface of the polymer filaments prior to the ME process, the former were uniformly embedded on the adlayer of the latter during layer-by-layer solidification after thermal diffusion. Chronologically, according to the channel flow dynamics in which the shear stress decreased exponentially, passing toward the center, i) the ceramic nanoparticles shallowly penetrated the diffusive environment created by the fluidic polymer before slightly dispersing toward areas with a low shear rate to avoid abrasion and friction between the liquid polymer and heated nozzle.[6,39] During the process, ii) nanoparticle agglomeration was separated to create further segmented and divided states because the repulsive van der Waals forces and interactions between the solid ceramic and liquid polymer, such as high surface charge, double layer formation, and steric force, were more dominant, thereby forming a highly uniform $TiO_2$ nanoparticle layer inside the adlayer.[6,25,40] However, iii) the ceramic nanoparticles could reversibly float toward the adjacent surface (adlayer) of the polymeric substance as a solid because of the suspension-balancing effect.[25,41] Simultaneously, there were no chemical reactions between the ceramic reinforcement and polymeric matrix; thus, the $TiO_2$ nanoparticles agglomerated into their original state via van der Waals interactions, which decreased the surface energy.[40] After expulsive migration

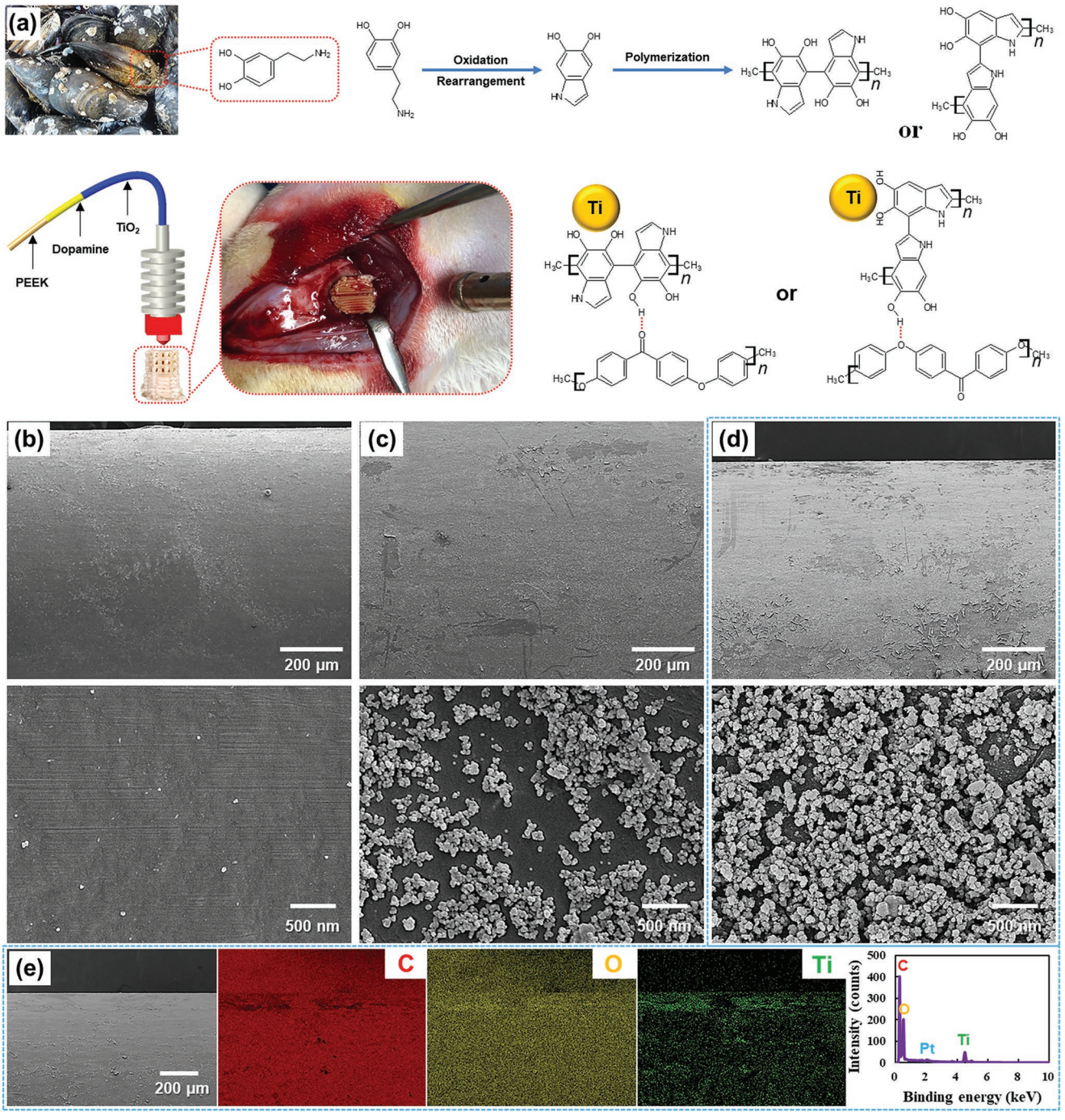


**Figure 1.** Application of mussel-inspired dopamine chemistry with ME to fabricate PEEK/$TiO_2$ composite implants. a) A photograph of mussels and a schematic to illustrate the use of 3,4-dihydroxyphenylalanine from their adhesive protein, which played an important role in the interfacial bonding of $TiO_2$ nanoparticles to PEEK filaments, which were used as an orthopedic implant in the rabbit femur (second photograph). Low- and high-magnification SEM images of b) a pristine PEEK filament and PEEK/$TiO_2$ filaments covered with c) 1.78 wt.% or d) 4.48 wt.% $TiO_2$ nanoparticles. The PEEK filaments were covered with a high fraction of $TiO_2$ nanoparticles up to the point of saturation due to their strong grafting onto the PEEK filament surfaces through the polydopamine adhesive. e) An SEM image of a PEEK/$TiO_2$ filament covered with 4.48 wt.% $TiO_2$ nanoparticles, along with corresponding elemental mapping images for C, O, and Ti and an EDS spectrum.

(suspension-balancing effect) toward the PEEK adlayer in the diffusive environment of the polymer fluid, ceramic agglomeration became more prevalent on the solidified polymer, thereby forming a constrained protuberant morphology of the structure (Figure S2c,d, Supporting Information).[6,25] Thus, while there was a conflict between the channel flow dynamics and suspension-balancing model (**Figure 2**a), which would tend to transport the ceramic nanoparticles toward the interior

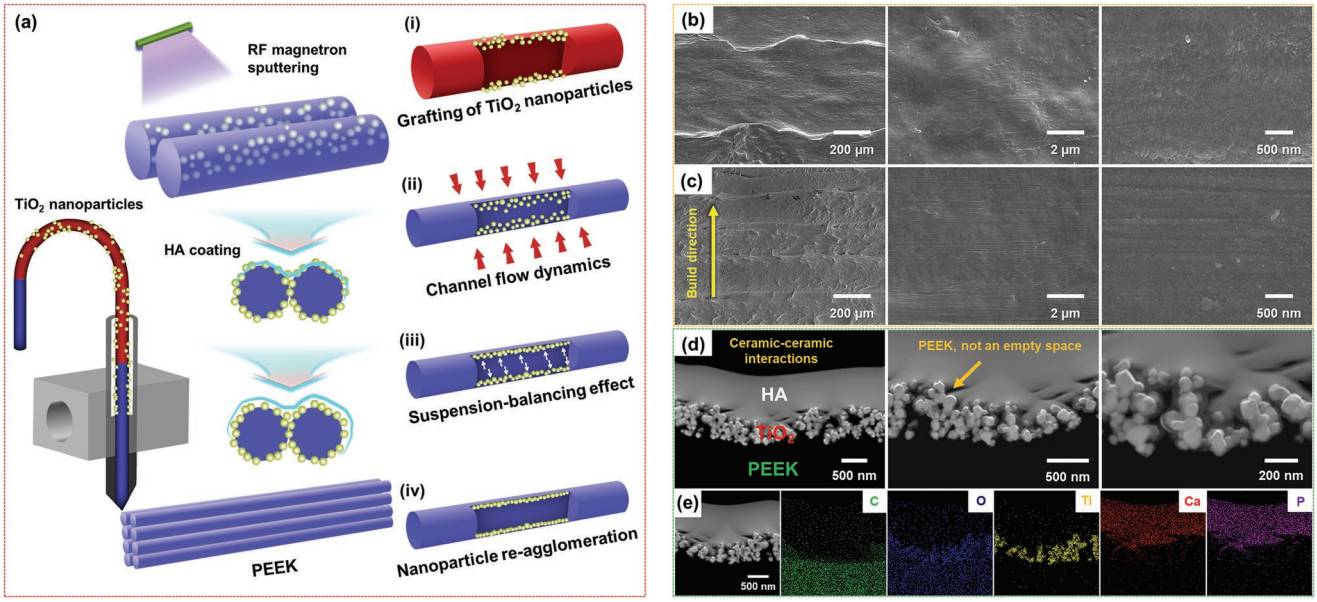


**Figure 2.** Equilibrium between the channel flow dynamics and the suspension-balancing effect on nanoparticle dispersion and agglomeration in the PEEK/$TiO_2$ composite. a) The mechanism of internal $TiO_2$ reinforcement and external HA coating on the PEEK matrix: (i) initial distribution of $TiO_2$ nanoparticles at the uppermost surface of the PEEK filaments; (ii) penetration and scattering of $TiO_2$ nanoparticles in the deep region during extrusion through the narrow printing nozzle; (iii) migration of $TiO_2$ nanoparticles to the outer surface via the suspension-balancing effect; and (iv) dispersion and densification of $TiO_2$ nanoparticles in the adlayer during agglomeration. b) Top-view and c) side-view SEM images of the PEEK/$TiO_2$/HA hybrid composite reinforced with 4.41 wt.% $TiO_2$ nanoparticles and sputtered with 1.56 wt.% HA. The $TiO_2$ nanoparticles were uniformly prevalent along the surface of the PEEK matrix, while the HA coating infilled the nanoscale protuberances on the PEEK/$TiO_2$ composite. As a result, the PEEK/$TiO_2$/HA hybrid composite had a much less rugged surface that was fully covered by the HA coating, regardless of the surface state of the PEEK/$TiO_2$ composite with a coarse morphology. d) Cross-sectional STEM images of the hybrid composite reinforced with the band of $TiO_2$ nanoparticles and encapsulated with HA. The intermediate $TiO_2$ nanoparticles were tightly embedded in the PEEK adlayer without any deficiencies (pores, cracks, and defects), while the external HA shell strongly adhered to the surface of the PEEK/$TiO_2$ composite. e) A STEM image and corresponding elemental mapping images of the interfaces of the PEEK/$TiO_2$/HA hybrid composite indicating the chemical compositions of each constituent.

and surface of the matrix, respectively, the ceramic reinforcement became rapidly consolidated in an intermediate adlayer of the polymeric matrix. Consequently, the adjacent surface of the polymer was stabilized by the dispersant layer of the ceramic nanoparticles. In the face of these specific interactions, the $TiO_2$ nanoparticles were uniformly distributed on the PEEK adlayer, despite reversible nanoparticle agglomeration, and thus exhibited nanoscale protuberances on the surface of the PEEK/$TiO_2$ composite. Subsequently, the HA coating was tightly attached to the rugged exterior of the PEEK/$TiO_2$ composite (Figure S2c,d, Supporting Information) after RF magnetron sputtering, which transformed the surface morphology by creating a much less rugged surface in the PEEK/$TiO_2$/HA hybrid composite (Figure 2b,c). In fact, after the ceramic nanoparticles had further separated on the polymeric substance, the HA coating filled and packed the deficiencies (pores and cracks) while thoroughly encapsulating the empty spaces in the PEEK/$TiO_2$ composite, which alleviated the surface energy of the latter (Figure 2d; Figure S2g,h, Supporting Information). Moreover, energy-dispersive X-ray spectrometry (EDS) analysis of the interfaces exhibited that there were no chemical reactions among the constituents of the hybrid composite, retaining their chemical compositions (Figure 2e), which were determined more distinctly using X-ray diffraction (XRD) and X-ray photoelectron spectroscopy (XPS) analyses. The elemental mapping images show the presence of the three different constituents, including PEEK with high amounts of C and O, $TiO_2$ with high amounts of Ti and O, and HA with high amounts of Ca, P, and O. Thus, O was commonly present in all three constituents. Overall, although a rough conformation was present on the surface of the PEEK/$TiO_2$ composite due to the agglomeration of embedded $TiO_2$ nanoparticles on the solidified PEEK via heterogeneous ceramic-polymer adherence, the ceramic nanoparticles favored tight interlocking when the HA was sputtered on the coarse nanoscale surface of the PEEK/$TiO_2$ composite due to homogeneous ceramic-ceramic coherence.

### 2.3. Microscopic and Spectroscopic Analyses of Each Constituent in the PEEK/$TiO_2$/HA Hybrid Composite

**Figure 3**a shows a low-magnification transmission electron microscopy (TEM) image of $TiO_2$ nanoparticles embedded on the PEEK filaments followed by coating with HA. The complex interfacial boundaries explain the main presence of the PEEK phase adjacent to the tightly bound $TiO_2$ phase and the thinly coated HA phase. The polycrystalline structures of $TiO_2$ and HA, as well as the amorphous structure of PEEK, formed distinct interfaces. Furthermore, lattice fringe measurements of each constituent indicate their combined presence. The chemical composition of each constituent in the hybrid composite is distinctly defined in the selected-area electron diffraction

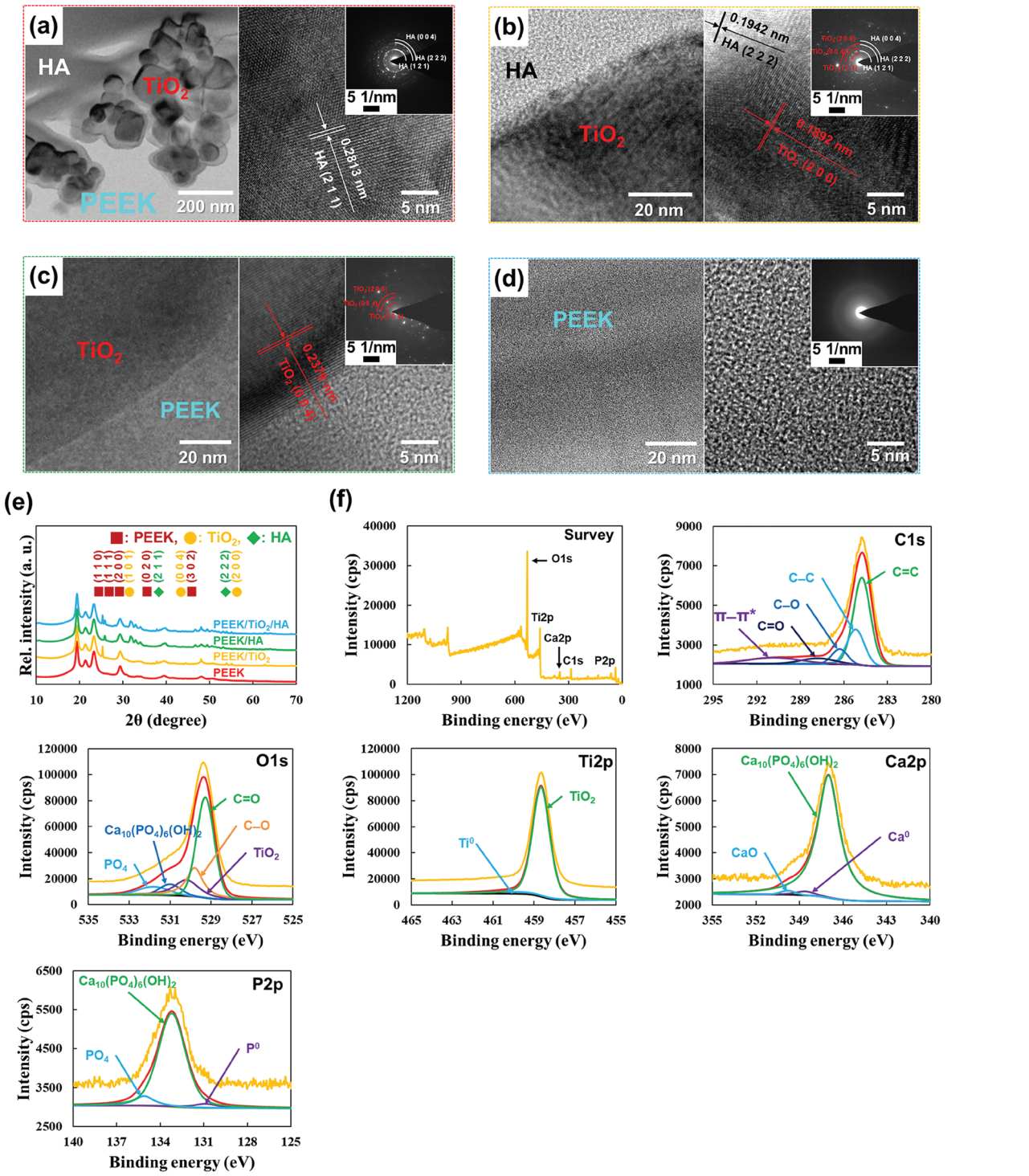


**Figure 3.** Microscopic images and spectroscopic analyses of each constituent in the PEEK/$TiO_2$/HA hybrid composite. a) A low-magnification TEM image showing distinctive interfacial boundaries for each of the PEEK/$TiO_2$/HA hybrid composite constituents and a high-resolution TEM image of HA with lattice fringe measurements. The inset shows the SAED pattern of the corresponding region. Intermediate- and high-resolution TEM images of b) $TiO_2$/HA, c) $TiO_2$/PEEK, and d) PEEK, with lattice fringe measurements. The insets in the high-resolution images show the SAED patterns of the corresponding regions. e) XRD spectra of the standard PEEK, the PEEK/$TiO_2$ composite incorporated with 4.48 wt.% $TiO_2$ nanoparticles, the PEEK/HA composite coated with 1.56 wt.% HA, and the PEEK/$TiO_2$/HA hybrid composite reinforced with 4.41 wt.% $TiO_2$ nanoparticles and coated with 1.56 wt.% HA. The presence of PEEK was obvious, while the presence of the $TiO_2$ nanoparticles and the HA layer was ambiguous in the spectroscopic analysis due to the low concentrations of these components. f) XPS survey and high-resolution C1s, O1s, Ti2p, Ca2p, and P2p scans of the PEEK/$TiO_2$/HA hybrid composite reinforced with 4.41 wt.% $TiO_2$ nanoparticles and covered with 1.56 wt.% HA. The chemical state of each constituent is present in the spectroscopic analysis; thus, chemical reactions did not occur among the constituents of the hybrid composite.

(SAED) pattern. Specifically, the presence of HA with a sharp ring pattern (polycrystalline) is shown in the inset of Figure 3a, the sharp ring pattern of HA and the ring pattern of $TiO_2$ at the interfacial boundary are shown in the inset of Figure 3b, the ring pattern of $TiO_2$ and the halo pattern indicating the amorphous structure of PEEK at the interfacial boundary are shown in the inset of Figure 3c, and the presence of PEEK with the halo pattern is shown in the inset of Figure 3d. The four SAED patterns confirm the presence of each constituent in the orthopedic implant. However, no new patterns appeared at the interfacial boundaries. Thus, there were no chemical reactions among the constituents during ME and RF magnetron sputtering, which tightly bound the PEEK phase with both the $TiO_2$ and HA phases.[6,25] Furthermore, the presence of both $TiO_2$ and HA on the PEEK surface was confirmed via XRD and XPS analyses. The elemental compositions and crystalline structures of PEEK, PEEK/$TiO_2$, PEEK/HA, and PEEK/$TiO_2$/HA were characterized by XRD (Figure 3e). For the conventional PEEK substance after ME at 410 °C, the $2\theta$ values at 19.40°, 21.38°, 23.28°, and 29.46° corresponded to the (1 1 0), (1 1 1), (2 0 0), and (2 1 1) planes of PEEK, respectively. For the PEEK/$TiO_2$, three new peaks appeared at the $2\theta$ values of 25.31°, 37.79°, and 48.04°, which corresponded to the (1 0 1), (0 0 4), and (2 0 0) planes, respectively. These results are consistent with the body-centered tetragonal structure of $TiO_2$ (JCPDS 78–2486). As for the PEEK/$TiO_2$/HA hybrid composite, the featured diffraction peak of HA was present at ≈25.94° with a relatively strong intensity, but with a slightly broad band next to the peak at 25.31° for $TiO_2$. These results indicate that both $TiO_2$ and HA were successfully incorporated onto the 3D-printed PEEK material, as each constituent in the PEEK/$TiO_2$/HA hybrid composite was present. XPS was conducted to obtain more details of the chemical state of each constituent in the PEEK/$TiO_2$/HA hybrid composite. Figure 3f shows the survey spectrum of the $TiO_2$-reinforced and HA-coated PEEK hybrid composite, which mainly consisted of the C1s and O1s bands of PEEK; the Ti2p and O1s bands of $TiO_2$; and the Ca2p, P2p, and O1s bands of HA. According to the elemental composition analysis, the PEEK/$TiO_2$/HA hybrid composite was composed of 78.9 wt.% C, 17.0 wt.% O, 2.8 wt.% Ti, 0.8 wt.% Ca, and 0.5 wt.% P, which is consistent with the inductively coupled plasma-optical emission spectrometry (ICP-OES) results. In particular, the C1s band of the PEEK/$TiO_2$/HA hybrid composite was deconvoluted to provide three different peaks with specific binding energies (284.76 eV for C=C bonding, 285.22 eV for C−C bonding, and 286.18 eV for C−O bonding). For the O1s band, five different peaks at 529.28, 529.98, 530.12, 531.13, and 531.78 eV were attributed to the C=O, C−O, O=Ti=O, $Ca_{10}(PO_4)_6(OH)_2$, and $PO_4$ states, respectively. Subsequently, an analysis of PEEK with $TiO_2$ reinforcement was conducted to ascertain the chemical states of the Ti2p band and to show that no reactions occurred among PEEK, $TiO_2$, and HA. Hence, the Ti2p band showed only a single broad peak at a binding energy of 458.63 eV, which indicates the presence of $TiO_2$ only. Similarly, the XPS results for the HA surface signify that HA did not react with PEEK or $TiO_2$. Hence, the constituents of the hybrid composite retained their specific chemical compositions, and thus their individual properties, with no chemical reactions having occurred among them, which is in agreement with the results of XRD.

### 2.4. Enhanced Mechanical Properties of the PEEK/$TiO_2$/HA Hybrid Composite

**Figure 4**a indicates that PEEK reinforced with $TiO_2$ nanoparticles and coated with HA had an increased Vickers hardness compared with conventional PEEK. This can be explained by the internal $TiO_2$ reinforcement in the soft PEEK matrix and the external HA coating, which have much greater hardness values (951.1 and 535.0 HV, respectively) than PEEK (25.8 HV).[6,42,43] Although the pristine PEEK filaments were well fused at 410 °C (thereby achieving unexpectedly high intrinsic hardness), the hardness of the hybrid composite increased in proportion to the extent of $TiO_2$ reinforcement and HA coating, mainly because they tightly and densely bound to the PEEK matrix via physical interactions.[6]

Figure 4b–e shows the tensile and compression test results of the 3D-printed PEEK materials with 1.78 or 4.48 wt.% TiO2 reinforcement and 0.85 or 1.56 wt.% HA coating. In particular, the PEEK/$TiO_2$/HA hybrid composite reinforced with 4.41 wt.% $TiO_2$ nanoparticles and sputtered with 1.56 wt.% HA had higher tensile and compression elastic modulus values (4.5 and 5.5 GPa, respectively) than conventional 3D-printed PEEK (3.4 and 4.1 GPa, respectively) due to the strong physical interactions among the constituents. However, because the $TiO_2$ and HA ceramics did not chemically react with the PEEK polymer despite their uniform distribution at 410 °C and subsequent dense sputtering (coating) on the PEEK/$TiO_2$ composite, the elongation values at fracture of the composites and hybrid composites were similar or slightly lower after increasing the reinforcement amount and coating thickness. Meanwhile, although all of the samples were built layer-by-layer at the same temperature and speed in the longitudinal direction, their binding efficiencies in addition to the incorporated $TiO_2$ nanoparticles and the HA coating thickness on 3D-printed PEEK significantly influenced the tensile and compression properties of the additively manufactured hybrid composites.

As shown in Figure 4f, the adherence stability of both $TiO_2$ reinforcement and HA coating (or either one of them) on 3D-printed PEEK was quantified through scratch testing to determine how strongly the reinforcement and coating resisted exfoliation during adhesive failure. In particular, $TiO_2$ nanoparticles were mostly distributed in the adlayer of the PEEK/$TiO_2$ composite with an intensely roughened surface morphology. In terms of delamination resistance, the protrusions of the PEEK/$TiO_2$ composite improved the adhesion stability of the densely distributed HA coating via strong mechanical interlocking. In general, this mechanical anchoring effect can reduce the stress concentration at the coating-substance interface and decrease the interfacial fracture energy of the coating under mechanically challenging conditions.[6] Meanwhile, Figure 4g shows the coefficient of friction (COF) of the plain substance, the composites, and the hybrid composites under variable force ranging from 0.00 to 5.00 N and a straight scratch track of 1.00 mm with a Rockwell diamond stylus. Initially, the COF of standard PEEK increased gradually from 0.001 to a maximum of 0.015 within 1.00 mm until the end of the test due to a constant increase in the contact area, despite a slight fluctuation at ≈0.45 mm. Conversely, the excellent abrasion and scratch resistance of the $TiO_2$-reinforced composites and the HA-coated

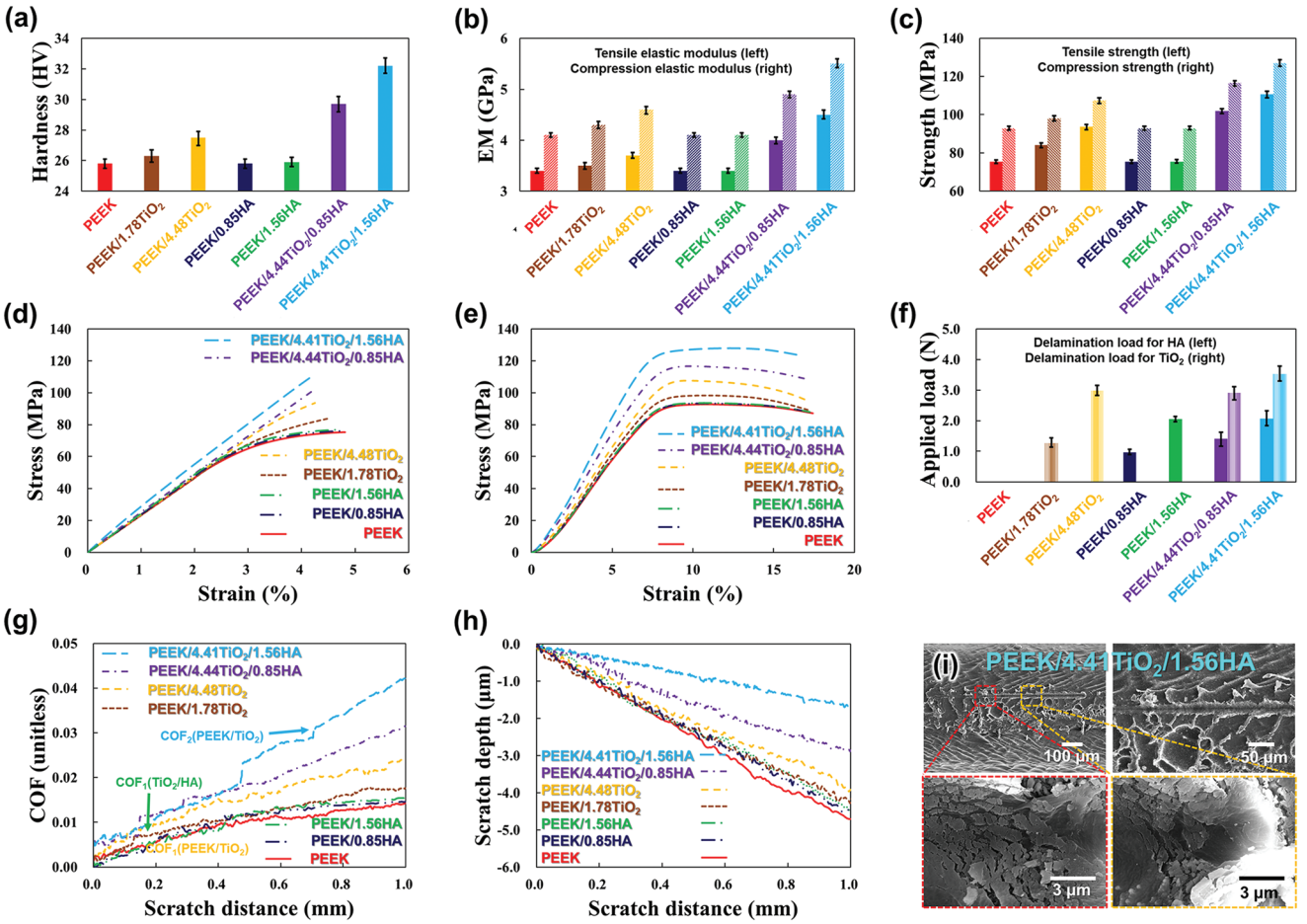


**Figure 4.** Mechanical strength comparison of conventional PEEK, the PEEK/$TiO_2$ composite incorporated with 1.78 or 4.48 wt.% $TiO_2$, the PEEK/HA composite sputtered with 0.85 wt.% or 1.56 wt.% HA, and the PEEK/$TiO_2$/HA hybrid composite internally reinforced with 4.44 or 4.41 wt.% $TiO_2$ and externally coated with 0.85 or 1.56 wt.% HA, respectively. a) Vickers hardness, b) elastic modulus, and c) strength measurements from the d) tensile and e) compression tests. f) Applied load in the g) coefficient of friction (COF) and h) scratch depth results through scratch testing. Encapsulation with HA rather than reinforcement with $TiO_2$ more effectively improved the mechanical strength of the hybrid composite relative to conventional PEEK. i) SEM images of the scratched area on the PEEK/$TiO_2$/HA hybrid composite internally reinforced with 4.41 wt.% $TiO_2$ and externally coated with 1.56 wt.% HA showing the highest mechanical strength. All the hardness and tensile and compression test results are expressed as mean ± standard deviation (n = 5); however, the representative graphs of the tensile and compression and scratch test results were present on the figure. Each *p*-value of < 0.05 per the experiment was considered statistically significant.

hybrid composites resulted in higher COF values than non-reinforced PEEK because the $TiO_2$ nanoparticles, which were tightly embedded on the adjacent surface of PEEK, gave rise to more intense friction between the reinforcement on the matrix and stylus. In particular, the critical COF [COF1(PEEK/$TiO_2$)] was signified by an abrupt increase from 0.005 to 0.008 at 0.10 mm, which indicates exfoliation of $TiO_2$ nanoparticles with a thickness of 410 nm embedded on the rough surface of PEEK. A small degree of fluctuation occurred due to the relatively weak ceramic-polymer interactions between the $TiO_2$ nanoparticles and 3D-printed PEEK. In addition to the reinforcement effect, the COF of the hybrid composites coated with 0.85 or 1.56 wt.% HA was even higher due to encapsulation, which enabled more frequent and deeper grooves during testing. Although there were two violent fluctuations in COF at critical scratch depths for both of the PEEK/$TiO_2$/HA hybrid composites coated with 0.85 and 1.56 wt.% HA, respectively (one due to $TiO_2$ reinforcement [COF2(PEEK/$TiO_2$)] and the other due to HA coating [COF1($TiO_2$/HA)]), the peak for the first fluctuation was higher than that of the second fluctuation. This is because the bonding of the HA coating with the $TiO_2$ nanoparticles via strong ceramic-ceramic interactions is more robust than the bonding of the $TiO_2$ nanoparticles with the 3D-printed PEEK, which occurs via relatively weak ceramic-polymer interactions. Scratch depth measurements (Figure 4h) explain the reinforcement effect of $TiO_2$ nanoparticles in the composites and hybrid composites, as well as the encapsulation effect of HA on the latter. The standard substance had a relatively weak scratch resistance (adhesion strength); the scratch depth gradually deepened from –0.01 to –4.70 μm within 1.00 mm and slightly fluctuated during part of the abrading time. This was attributed to the poor scratch resistance of conventional PEEK, overlapping of melted PEEK filaments, and the presence of pores and/or defects formed during ME. After addition of 1.78 or 4.48 wt.% $TiO_2$ nanoparticles to the PEEK filaments, the scratch depths in the composites were slightly shallower than

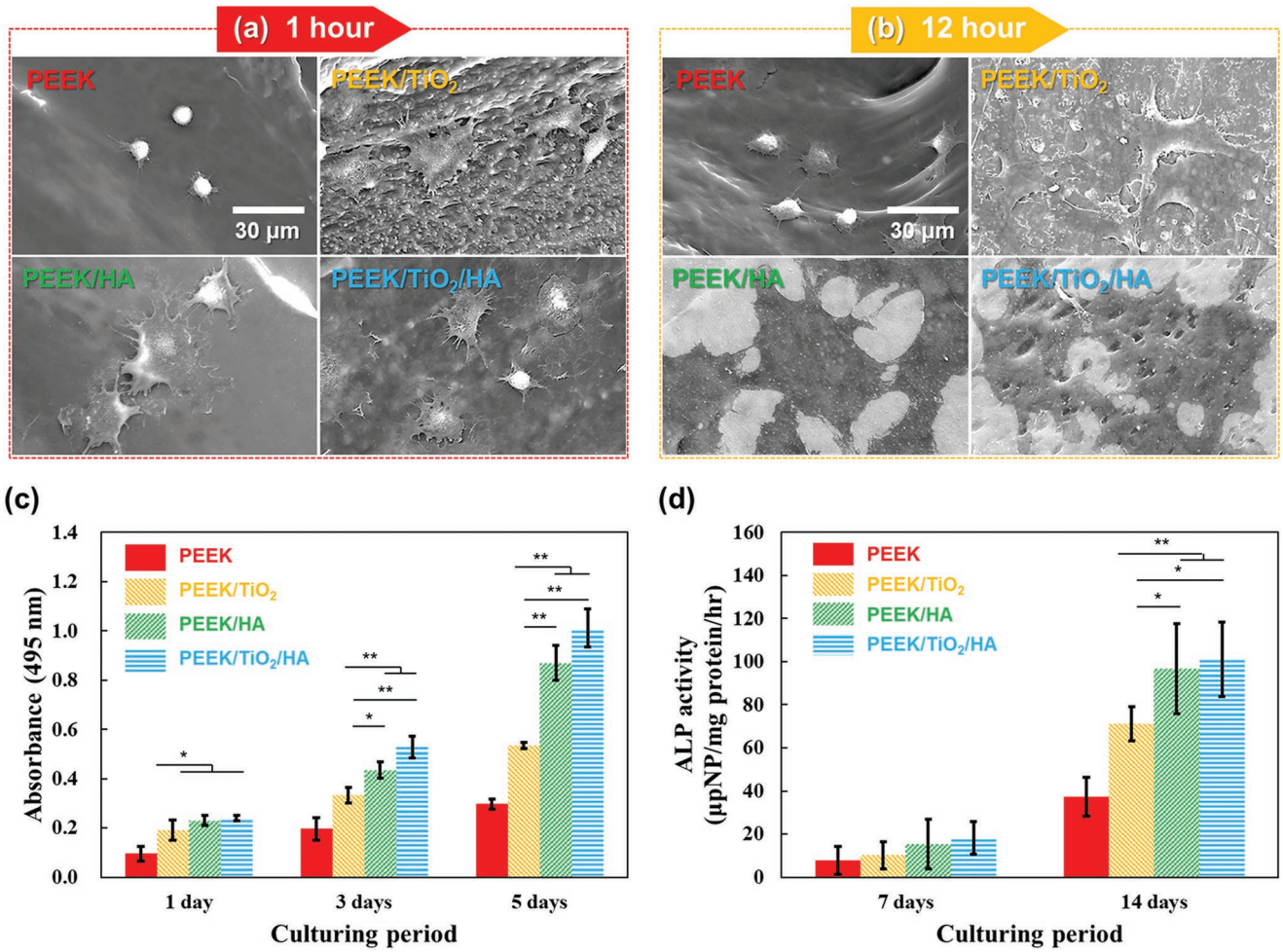


**Figure 5.** Evaluation of the bioactivity of various scaffold materials in vitro. SEM images of adhered MC3T3–E1 cells on the surfaces of the PEEK, PEEK/$TiO_2$, PEEK/HA, and PEEK/$TiO_2$/HA scaffolds after culturing for a) 1 h and b) 12 h. c) Cell viability and d) ALP activity of MC3T3–E1 cells on the bioscaffolds after culturing for 1, 3, and 5 days, and 7 and 14 days, respectively. $^{*}p < 0.05$; $^{**}p < 0.01$.

those in the conventional 3D-printed PEEK (–3.92 μm with 4.48 wt.% $TiO_2$ reinforcement during the entire 1.00 mm process), which confirmed the reinforcement effect of the $TiO_2$ nanoparticles. Thus, the composites were relatively stable with shallower scratch depths than the non-reinforced PEEK. Finally, the scratch depths of the hybrid composites coated with 0.85 or 1.56 wt.% HA were even shallower, albeit with marked initial fluctuations. In particular, the final scratch depth of the hybrid composite with a 1.56 wt.% HA coating was much shallower (–1.75 μm) than that of the PEEK/$TiO_2$ composite reinforced with 4.48 wt.% $TiO_2$ nanoparticles (–3.92 μm), which was previously explained by the fact that the bonding of the HA coating with the $TiO_2$ nanoparticles via ceramic-ceramic interactions is stronger than the bonding of the $TiO_2$ nanoparticles with the 3D-printed PEEK via ceramic-polymer interactions.

### 2.5. Bioactivity Evaluation of the Scaffolds In Vitro

The in vitro biological properties of the additively manufactured PEEK, PEEK/$TiO_2$ composite, PEEK/HA composite, and PEEK/$TiO_2$/HA hybrid composite scaffolds were compared by measuring cell attachment, proliferation, and differentiation. The scanning electron microscopy (SEM) images in **Figure 5**a,b show the morphologies of the preosteoblasts adhered to each bioscaffold after 1 and 12 h of culturing, respectively. Only a few cells retaining their spherical shape were spread on the surface of the pristine PEEK scaffold, and the number of cells did not change with an increase in culture time. In contrast, many cells were tightly adhered and widely spread out on the surface of the PEEK/HA composite scaffold after 1 h of culturing, with numerous filopodia-like cell protrusions, leading to substantial cell spreading after culturing for 12 h. Although the PEEK/$TiO_2$ composite scaffold also exhibited high cellular adhesion behavior that was comparable to that of the PEEK/HA composite scaffold, the HA coating further improved the cell spreading area and adhesion after 12 h of culturing. Alkaline phosphatase (ALP) and 3-(4,5-dimethylthiazol-2-yl)-5-(3-carboxymethoxyphenyl)-2-(4-sulfophenyl)-2H-tetrazolium (MTS) assays were performed to evaluate the differentiation and proliferation, respectively, of preosteoblasts on the additively manufactured bioscaffolds.[14,44–46] As shown in Figure 5c,

cell proliferation on all bioscaffolds increased after culturing for 5 days, thereby signifying bioscaffold cytocompatibility. Meanwhile, cells cultured on the PEEK/$TiO_2$ composite scaffold proliferated more rapidly than those on the pristine PEEK scaffold, which demonstrated the lowest cellular proliferation rate among all of the bioscaffolds. The cell proliferation rates on the PEEK/HA composite and PEEK/$TiO_2$/HA hybrid composite scaffolds were the fastest at all time points and were markedly higher than the cell proliferation rate on the PEEK/$TiO_2$ composite scaffold. The differences between the HA-coated and non-coated scaffolds gradually increased with an increase in culture time. This trend was also observed in the cell differentiation assay (Figure 5d). Among the four scaffolds, the two HA-coated scaffolds had the highest ALP activities for the first 14 days, although the differences among the bioscaffolds on day 7 were not statistically significant. the differences in the in-vitro cellular responses between the HA-coated and non-coated scaffolds increased with an increase in culture time. This outstanding cellular response is attributable primarily to the hydrated surface layer of HA and the presence of cell-binding ionic sites, such as calcium cations and phosphate anions. Consequently, preosteoblasts were able to readily adhere to and spread over the surface during the early stages of cell growth, leading to more prevalent osteoblast differentiation.[23]

### 2.6. In Vivo Comparison of Bone Regeneration and Osseointegration of the Implants Fabricated from the Various Materials

The implants fabricated from the various materials were explicitly designed to include porous lower regions and dense upper regions to evaluate bone regeneration and bone-to-implant contact rates. Because RF magnetron sputtering is a line-of-sight process, the HA coating was mostly formed on the outer surfaces of the additively manufactured implants, and only half of their surfaces were covered to directly compare the bone tissue response with and without HA coating.[47] As shown in **Figure 6**, each implant was inserted into the individual rabbit distal femur defect, and after 4 and 8 weeks, the new bone regeneration volume inside the porous region was assessed using micro-CT. Figure 6a,b shows representative 3D images of new bone formation from that the volume was quantitatively assessed. The pristine PEEK and PEEK/$TiO_2$ composite implants had significantly lower signal intensities than bone cells and tissues, so they were not visible on micro-CT images. Although all implants revealed more new bone formation with time after implantation, substantial differences existed between those with and without $TiO_2$ nanoparticles (Figure 6c). The pristine PEEK and PEEK/HA composite implants showed the lowest bone volumes at each time point in the post-implantation period, and the HA coating did not significantly influence the rate of bone regeneration inside the pores of these implants. In contrast, the PEEK/$TiO_2$ composite implant exhibited a significantly improved bone regeneration ability, which was 2–6 times higher than the standard PEEK and PEEK/HA composite implants at 4 and 8 weeks after implantation. Moreover, the volume and thickness of new bone in the PEEK/$TiO_2$/HA hybrid composite implant were greater than in the PEEK/$TiO_2$ composite implant at 4 and 8 weeks after implantation, and the quantitative analysis showed that the new bone volume was substantially greater than in the other implants.

Bone-to-implant contact was closely examined by histology of the dense upper regions on the implant surfaces, which were designed to fix the implants and provide close contact between the implants and surrounding bone. As shown in **Figure 7**a,b, all of the additively manufactured implants exhibited cross-sectionally uneven threads that were in close contact with the bone on that newly formed bone tissue gradually formed. There were clear histological differences between the PEEK and PEEK/$TiO_2$ composite implants. At 8 weeks after implantation, only a small proportion of the PEEK implant surface was covered with soft tissue. In contrast, bone tissue regeneration inside the PEEK/HA composite implant was negligible. Thus, both the PEEK and PEEK/HA implants showed almost undetectable new bone formation inside the pores nearest to surrounding bone, which supported the micro-CT observations. In contrast, the PEEK/$TiO_2$ composite and PEEK/$TiO_2$/HA hybrid composite implants showed gradually increasing new bone regeneration in the pores according to the post-implantation time. In particular, new bone regeneration with the hybrid composite implant was considerably greater than that of the other implants at 8 weeks after implantation (Figure 7c). Furthermore, the hybrid composite implant had almost the same number of bone-to-implant contacts as the PEEK/HA composite implant at 4 and 8 weeks after implantation (Figure 7d). The main reason for this excellent bone tissue response to the HA coating is the coating's similar mineral composition to natural bone, which facilitates bone cell adhesion and growth, thus ensuring direct bone deposition on its surface.[23,47] Furthermore, HA's active role in upregulating bone metabolism and regeneration is well known. This undoubtedly led to the improvement in new bone formation, even in the pores of the PEEK/$TiO_2$/HA hybrid composite implant, compared with the PEEK/$TiO_2$ composite implant.[23,47] Consequently, the results of our histomorphometric evaluation revealed that the HA coating was highly effective at enhancing bone deposition directly on the implant surfaces. Thus, $TiO_2$ reinforcement and HA coating provided complementary and synergistic effects on new bone formation, even inside the pores.

## 3. Conclusions

The PEEK/$TiO_2$/HA hybrid composite demonstrated significantly greater mechanical strength than the conventional PEEK owing to its complementary $TiO_2$ reinforcement and synergistic HA coating. The hardness, tensile and compressive strength, and scratch resistance (adhesion strength) of the hybrid composite were improved by heat treatment at a high temperature of 410°C during ME because the internal $TiO_2$ reinforcement became tightly bound within the soft PEEK matrix, after that the external HA coating strongly adhered to the surface of the PEEK/$TiO_2$ composite. From a biocompatibility perspective, the histological results of a microscopic analysis of cultured cells demonstrated the strong potential of the PEEK/$TiO_2$/HA hybrid composite to support cellular integration, sustainability, and proliferation when used as an orthopedic scaffold material. The feasibility and usefulness of the PEEK/$TiO_2$/HA hybrid composite tailored as an orthopedic implant were successfully

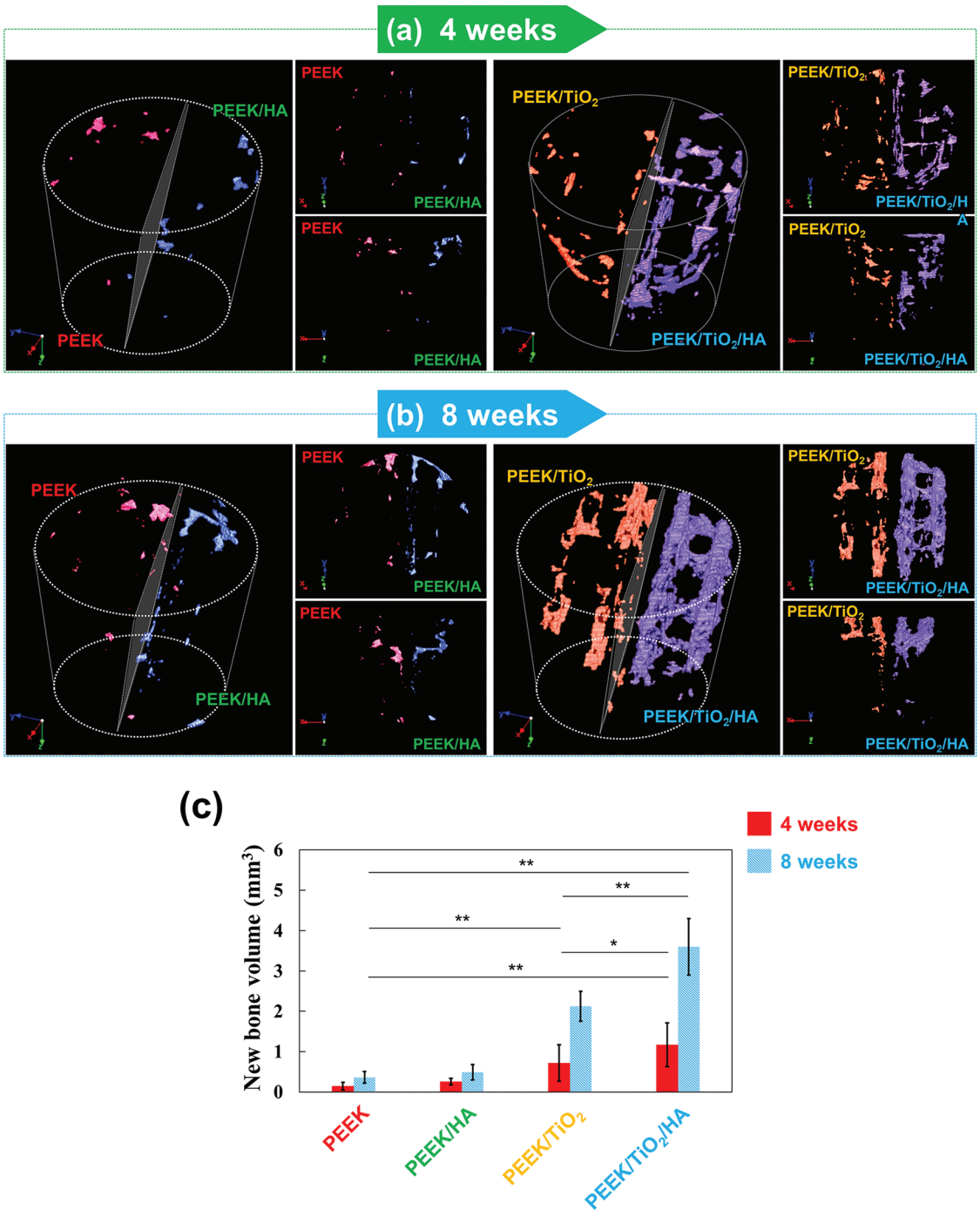


**Figure 6.** Evaluation of in-vivo bone regeneration and osseointegration inside the various implants. 3D micro-CT images of regenerated bone inside the porous regions of the PEEK, PEEK/$TiO_2$, PEEK/HA, and PEEK/$TiO_2$/HA implants at a) 4 and b) 8 weeks after implantation, along with c) new bone volume measurements. *$p$< 0.05; **$p$ < 0.01.

demonstrated by its insertion into the femur of rabbits in vivo, and new bone regeneration without inflammation or infection in the contact area was evident even after 1 month. Overall, the $TiO_2$ nanoparticle-reinforced and HA-coated bioimplant with high strength and biocompatibility, which was developed using an effective additive manufacturing process, represents a great advancement in the field of composite prostheses.

## 4. Experimental Section

*Immobilization of $TiO_2$ Nanoparticles on the Surfaces of PEEK Filaments*: Polyether ether ketone (PEEK) filaments with a diameter of 1.75 mm (PEEK 450 G) were purchased from Apium Additive Technologies GmbH (Germany). Dopamine hydrochloride, titanium(IV) isopropoxide, and tris(hydroxymethyl)aminomethane were obtained from Sigma–Aldrich (USA). Dopamine solution at a concentration of 6.0 g $L^{-1}$ was prepared

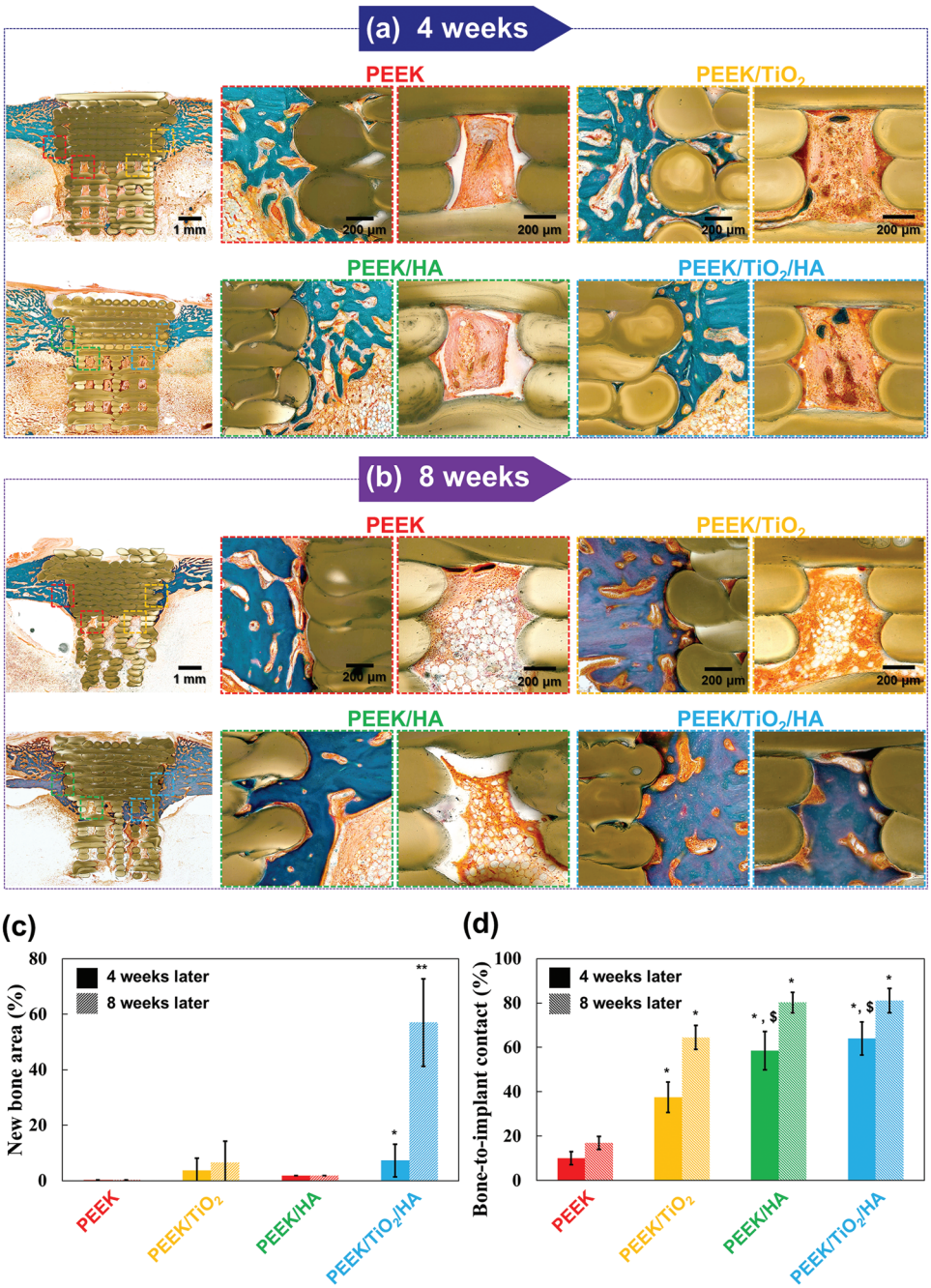


**Figure 7.** Qualitative histological observations and quantitative analyses of the contact points between the embedded implants and surrounding bone. Low- and high-magnification microscopic images of the surfaces and inside the pores of the PEEK, PEEK/$TiO_2$, PEEK/HA, and PEEK/$TiO_2$/HA implants removed from rabbits at a) 4 weeks and b) 8 weeks after implantation. Quantitative analyses of c) the new bone area inside the pores and d) the bone-to-implant contact ratio around the implant surfaces at 4 and 8 weeks after implantation. $^{*}p < 0.05$; $^{**}p < 0.01$.

by dissolving dopamine hydrochloride in distilled water. A bundle of PEEK filaments was added to the aqueous dopamine solution while stirring, and the solution was heated to 70 °C. After the predetermined time of 24 h, either 0.0, 4.0, or 8.0 g of titanium(IV) isopropoxide was added dropwise and allowed to dissolve. Immobilization (grafting) of the $TiO_2$ nanoparticles started on the surfaces of dopamine-functionalized PEEK filaments, and the pH was adjusted to 8.5 by adding 10 mM tris(hydroxymethyl)aminomethane solution. After grafting, each composite was washed with isopropanol and dried at 100 °C under vacuum for 3 h followed by characterization.

*Fabrication of the Additively Manufactured PEEK Orthopedic Implant with $TiO_2$ Reinforcement and HA Coating*: As the precursor material, pristine PEEK filaments at a density of 1.3 g $cm^{-3}$ were built layer-by-layer using a custom-made material extrusion (ME) printer (EP-300, Lincsolution, Inc., Korea).[14] More specifically, the PEEK filaments were extruded out of the printing head at a nozzle temperature of 410 °C, a chamber temperature of 160 °C, and with a nozzle diameter of 0.6 mm. The thickness of the printed layer was 0.2 mm, and the width was 0.4 mm. During printing, the liquefying head moved back and forth while filling out the predefined layers. The process was rapidly repeated,

eventually yielding a femur-specific orthopedic implant.[48] Subsequently, the composite implants were fabricated using PEEK filaments reinforced with different amounts of $TiO_2$ nanoparticles. The polydopamine derivatives, unreacted dopamine, and any impurities, which can cause unexpected metabolic disorders and neural system malfunctions, were degraded under a high-temperature heat treatment, leaving only the $TiO_2$ reinforcement and PEEK matrix. Finally, hydroxyapatite (HA) was coated on the surfaces of the PEEK/$TiO_2$ composites through radiofrequency (RF) magnetron sputtering (Vacuum Science Co., Korea) using a circular target with a diameter of 76 mm and a thickness of 6 mm. The additively manufactured substance was ultrasonically cleaned with ethanol for 10 min and loaded in a sputtering vacuum chamber with a working distance (distance between the substance and HA target) of 125 mm. The chamber was evacuated to a pressure of $\approx 9 \times 10^{-6}$ Pa, and Ar gas (99.999%) was introduced at a pressure of 1.3 Pa through a mass flow controller. Before the HA coating, the additively manufactured substance was further cleaned using Ar plasma by applying RF power at 50 W for 5 min, after which the HA target was sputtered for 4 h at $1.3 \times 10^{-1}$ Pa Ar atmosphere by applying RF power at 150 W.

*Characterization of the Additively Manufactured Orthopedic Implant*: The wt.% of C and O in the orthopedic implants was determined using a carbon/sulfur analyzer (CS–800, ELTRA GmbH, Germany) and an oxygen/nitrogen analyzer (ON–900, ELTRA GmbH) with a sensitivity of 0.01 ppm and an accuracy of ±0.1 ppm for a sample of 1.0 g.[49] The amounts of $TiO_2$ and HA were measured and calculated from the test results using inductively coupled plasma-optical emission spectrometry (ICP-OES; Optima 7300DV, PerkinElmer, USA).[50] The surface morphologies and chemical compositions of the filaments, plain substance, composites, and hybrid composites were examined with scanning electron microscopy (SEM; JSM–6701F, JEOL, Japan) equipped with energy-dispersive X-ray spectrometry (EDS) for elemental analysis.[51] The samples were prepared via a focused ion beam (AURIGA, Carl Zeiss, Germany) to investigate the distribution and thickness of the $TiO_2$ agglomeration and HA coating on the PEEK substance. Their detailed structures and compositions were also analyzed using transmission electron microscopy (TEM; Tecnai F30 S-Twin, FEI, USA) with selected-area electron diffraction (SAED). The crystalline structures of the implants were analyzed by X-ray diffraction (XRD; D/Max–2500VL/PC, Rigaku International Corporation, Japan). X-ray photoelectron spectroscopy (XPS; Quantera SXM, ULVAC–PHI, Japan) and the XPSPEAK 4.1 software were used to obtain more detailed information about the chemical states of the implant surfaces.

*Mechanical Testing of the Additively Manufactured Orthopedic Implant*: Vickers hardness was measured using a hardness tester (Duramin–40, Struers, Denmark) with a loading force of 9.807 N using a diamond stylus and a dwell time of 10 s. Each tensile (20 kN capacity and 5.0 mm $min^{-1}$) and compressive (20 kN capacity and 2.0 mm $min^{-1}$) test was carried out on identical tensile and compression testing machines (AGS–X, Shimadzu, Japan). Tensile testing was conducted in accordance with the American Society for Testing and Materials (ASTM) D638 regulation. The distance between the grips was 115 mm (following the rule for Type 1). For the molded specimen with a width of 13 mm in the gauge region, the area with a thickness of < 3.2 mm was also regulated. Air pressure was applied to appropriately grip the tensile specimen. However, the molded specimen can be damaged if held too tightly or slip if bound too loosely to the jaw jig. Scratch testing (DFM–0.5–G, Bruker Corporation, USA) was used to compare the adhesion strength of the standard 3D-printed PEEK with that of each composite and hybrid composite. The testing conditions using a diamond tip (12.5 µm radius with a hemispherical tip) were as follows: 0.10 mm $min^{-1}$ scratching speed, 0.00–5.00 N load force, and 0.05 N load resolution. The implant scratch depths were measured using a 3D profilometer (Contour GT–X, Bruker Corporation, USA).

*In Vitro Assays of the PEEK/$TiO_2$/HA Hybrid Composite*: For the in vitro tests, the additively manufactured biomaterials were cleaned with ethanol for 10 min and sterilized overnight by ultraviolet irradiation.[46] The pre-incubated MC3T3–E1 cells (passage number 10–20) were seeded onto the biomaterials at densities of $5 \times 10^4$, $2 \times 10^4$, and $1.5 \times 10^4$ cells $cm^{-2}$ for the cellular adhesion, proliferation, and differentiation assays, respectively, followed by culturing in a humidified carbon dioxide incubator at 37 °C. The culture medium consisted of alpha-minimum essential medium (catalog no. LM008-53, Welgene Co. Ltd., Korea), 5% fetal bovine serum (catalog no. 16000–044, GIBCO, USA), and 1% penicillin-streptomycin (catalog no. SV30010, HyClone, USA).[45] A mixture of 10 mM $\beta$-glycerophosphate and 50 µg $mL^{-1}$ ascorbic acid was added to the culture medium for the alkaline phosphatase (ALP) assay. The adhered cell morphologies were observed using SEM (JSM–6360, JEOL). After 1 and 12 h of culturing, the adhered cells were treated with 2.5% glutaraldehyde (catalog no. 340 855, Sigma Aldrich, USA) for 10 min, a graded ethanol series (70%, 90%, 95%, and 100%) for 10 min, and hexamethyldisilazane (Sigma Aldrich) for 10 min. After 1, 3, and 5 days of culture, the cell proliferation rate was examined by incubating the cell aliquots with 3-(4,5-dimethylthiazol-2-yl)-5-(3-carboxymethoxyphenyl)-2-(4-sulfophenyl)-2H-tetrazolium (catalog no. G3582, MTS; Promega, USA), followed by reading the absorbance of the samples at 495 nm using a microplate reader (Model 550, Biorad, USA).[52] After culturing for 7 and 14 days, ALP activity (an indicator of early osteoblastic differentiation) was assessed by adding *p*-nitrophenyl phosphate (catalog no. P7998, Sigma Aldrich, USA), which was proportionally converted to *p*-nitrophenol (pNP) in the presence of ALP, to the suspended cell aliquots and measuring the amounts of pNP generated on the implants by reading the absorbance at 405 nm using a microplate reader. The in vitro experimental data (MTS assay and ALP activity) were expressed as mean ± standard deviation (n = 5).

*Evaluation of In Vivo Bone Regeneration*: The in vivo animal experiments, including surgery and sacrifice, were approved by the Ethics Committee on Animal Experimentation of the Institutional Animal Care and Use Committee of GENOSS (GEN–IACUC–1911–01). In the rabbit femur defect model, bone regeneration in implants inserted in the femur of 12 New Zealand white rabbits (12 weeks, weight range: 3.0–3.5 kg, Kosabio, Korea) was evaluated in vivo. The implants were designed to be cylindrical (diameter: 5 mm; length: 6 mm) and included fully dense and porous bodies with lengths of 2 and 4 mm, respectively. The HA coating was applied to half of the outer surfaces of the implants. Animals were anesthetized via intramuscular injection of a combination of 0.5 mL zoletil (Virbac Lab., France) and 1.5 mL rompun (Bayer Korea, Korea), while 0.5 mL of lidocaine (Yuhan Corporation, Korea) was injected percutaneously for local anesthesia. A cylindrical hole with a diameter of 5 mm and a length of 8 mm was created in each distal femur using a handpiece drill, and an implant was placed in the defect. After surgery, the wound was carefully sutured with a polyglycolic acid suture (Surgisorb, Samyang, Korea), and gentamicin (Samu Median, Korea) was injected intramuscularly once per day for 3 days. At 4 and 8 weeks after implantation, the rabbits were sacrificed with carbon dioxide (Figure S4, Supporting Information). The implants with adjacent bone cells and tissues were extracted and fixed in 10% formaldehyde solution for 1 week. To evaluate bone ingrowth, the harvested implants were analyzed using micro-CT (Skyscan 1173, Skyscan, Belgium) at a resolution of 14 µm, a voltage of 90 kV, and a current of 99 µA.[44] 3D images of new bone formation within the implants were reconstructed using NRecon software (Skyscan, Belgium), and new bone formation volume was calculated using CTAn and CTVox 2.4 software (Skyscan). For histological analysis, the fixed specimens were embedded in resin (Technovit 7200 VLC, Kulzer, Germany), and 50 µm-thick slices were obtained using an Exakt cutting and grinding system (Exakt, Germany). After staining with Goldner's trichrome, microscopic features were examined using a panoramic digital slide scanner (Pannoramic 250 Flash III, 3DHISTECH Ltd., Hungary). For each implant, the new bone area and bone-to-implant contact ratio were measured in the pores nearest to the surrounding bone tissues and on the surfaces of the dense body regions, respectively, using digital image analysis software (3DHISTECH Ltd.). All in vivo experimental data are expressed as mean ± standard deviation (n = 5). The experimenter was

unaware of the animal's group during raw data calculation and data analysis.

*Statistical Analysis*: Each assay was performed at least five times, and SPSS v. 20 (SPSS Inc., USA) was used for statistical analyses. All experimental values are reported as mean ± standard deviation. Before analyzing differences of data, a normality of variables was tested with a Shapiro-Wilk test. One-way analysis of variance followed by Tukey's post-hoc analysis was used to test for statistically significant differences between groups. A $p$-value of $< 0.05$ was considered statistically significant.

## Supporting Information

Supporting Information is available from the Wiley Online Library or from the author.

## Acknowledgements

This work was results of a study on the "Leaders in Industry-university Cooperation 3.0" Project, supported by the Ministry of Education and National Research Foundation of Korea. In addition, this work was supported by the Catholic University of Korea, Research Fund, 2020, and the National Research Foundation of Korea (NRF) grant funded by the Korean government (MSIT) (2021R1A2C1091301), the Korean Fund for Regenerative Medicine funded by the Ministry of Science and ICT, and by the Ministry of Health and Welfare (2021M3E5E5096420, Republic of Korea).

## Conflict of Interest

Hae Lin Jang is a founder and owns equity in Curer. The other authors declare that they have no competing financial interests.

## Author Contributions

T.-S.J. and S.J.P. contributed equally to this work. T.-S.J. and S.J.P. wrote and edited the paper and contributed to all of the activities. J.E.L., J.Y., and S.-H.P. additively manufactured the orthopedic implant. M.B.-G.J., Y.W.K., C.A., and J.P.C. analyzed the structures using microscopic and spectroscopic analyses and measured their mechanical properties. T.-S.J. and H.-D.J. conducted the various in vitro and in vivo experiments. Y.Z., R.C.A., Y.Z., H.L.J., N.-J.C., H.-D.J., and S.H.K. contributed to the interpretation and discussion of the experimental results.

## Data Availability Statement

The data that support the findings of this study are available in the supplementary material of this article.

## Keywords

additive manufacturing, dopamine-induced polymerization, homogeneous ceramic–ceramic interactions, orthopedic implants, protuberant nanoscale topography

Received: June 16, 2022
Revised: August 4, 2022
Published online:

[1] K. Barri, Q. Zhang, I. Swink, Y. Aucie, K. Holmberg, R. Sauber, D. T. Altman, B. C. Cheng, Z. L. Wang, A. H. Alavi, *Adv. Funct. Mater.* **2022**, 2203533.
[2] X. Huang, J. Xing, Z. Wang, J. Han, R. Wang, C. Li, C. Xiao, F. Lu, J. Zhai, Z. Zhou, *Adv. Funct. Mater.* **2021**, *31*, 2106249.
[3] X. Jin, Y. Xiong, X. Zhang, R. Wang, Y. Xing, S. Duan, D. Chen, W. Tian, F. Xu, *Adv. Funct. Mater.* **2019**, *29*, 1807915.
[4] W. Huang, M. Shishehbor, N. Guarín-Zapata, N. D. Kirchhofer, J. Li, L. Cruz, T. Wang, S. Bhowmick, D. Stauffer, P. Manimunda, *Nat. Mater.* **2020**, *19*, 1236.
[5] S. C. Ligon, R. Liska, J. Stampfl, M. Gurr, R. Mülhaupt, *Chem. Rev.* **2017**, *117*, 10212.
[6] A. M. Díez-Pascual, M. Naffakh, C. Marco, G. Ellis, M. A. Gómez-Fatou, *Prog. Mater. Sci.* **2012**, *57*, 1106.
[7] Y. Zhang, J. Xu, Y. C. Ruan, M. K. Yu, M. O'Laughlin, H. Wise, D. Chen, L. Tian, D. Shi, J. Wang, *Nat. Med.* **2016**, *22*, 1160.
[8] P. Aspenberg, *Nature Reviews Rheumatology* **2014**, *10*, 386.
[9] E. A. Guzzi, M. W. Tibbitt, *Adv. Mater.* **2020**, *32*, 1901994.
[10] F. B. Torstrick, A. S. Lin, D. Potter, D. L. Safranski, T. A. Sulchek, K. Gall, R. E. Guldberg, *Biomaterials* **2018**, *185*, 106.
[11] S. Amin Yavari, S. M. Castenmiller, J. A. van Strijp, M. Croes, *Adv. Mater.* **2020**, *32*, 2002962.
[12] C. Stewart, B. Akhavan, S. G. Wise, M. M. Bilek, *Prog. Mater. Sci.* **2019**, *106*, 100588.
[13] Y. Shi, L. Wang, Y. Niu, N. Yu, P. Xing, L. Dong, C. Wang, *Adv. Funct. Mater.* **2018**, *28*, 1804483.
[14] H. Jung, T. Jang, J. E. Lee, S. J. Park, Y. Son, S. Park, *Biofabrication* **2019**, *11*, 045014.
[15] W. R. Walsh, N. Bertollo, C. Christou, D. Schaffner, R. J. Mobbs, *The Spine Journal* **2015**, *15*, 1041.
[16] J. Soto-Alvaredo, E. Blanco, J. Bettmer, D. Hevia, R. Sainz, C. López Chaves, C. Sánchez, J. Llopis, A. Sanz-Medel, M. Montes-Bayón, *Metallomics* **2014**, *6*, 1702.
[17] Y. Li, C. Wong, J. Xiong, P. Hodgson, C. Wen, *Journal of Dental Research* **2010**, *89*, 493.
[18] F. B. Torstrick, B. S. Klosterhoff, L. E. Westerlund, K. T. Foley, J. Gochuico, C. S. Lee, K. Gall, D. L. Safranski, *The Spine Journal* **2018**, *18*, 857.
[19] K. T. Kim, M. Y. Eo, T. T. H. Nguyen, S. M. Kim, *International Journal of Implant Dentistry* **2019**, *5*, 10.
[20] D. Martini, M. Fini, M. Franchi, V. De Pasquale, B. Bacchelli, M. Gamberini, A. Tinti, P. Taddei, G. Giavaresi, V. Ottani, *Biomaterials* **2003**, *24*, 1309.
[21] M. Geetha, A. K. Singh, R. Asokamani, A. K. Gogia, *Prog. Mater. Sci.* **2009**, *54*, 397.
[22] S. Wu, Z. Weng, X. Liu, K. Yeung, P. K. Chu, *Adv. Funct. Mater.* **2014**, *24*, 5464.
[23] G. L. Koons, M. Diba, A. G. Mikos, *Nat. Rev. Mater.* **2020**, *5*, 584.
[24] Y. Liu, D. Luo, X. Kou, X. Wang, F. R. Tay, Y. Sha, Y. Gan, Y. Zhou, *Adv. Funct. Mater.* **2013**, *23*, 1404.
[25] A. M. Díez-Pascual, A. L. Díez-Vicente, *ACS Appl. Mater. Interfaces* **2015**, *7*, 5561.
[26] T. Lu, J. Wen, S. Qian, H. Cao, C. Ning, X. Pan, X. Jiang, X. Liu, P. K. Chu, *Biomaterials* **2015**, *51*, 173.
[27] C. Wang, K. Lin, J. Chang, J. Sun, *Biomaterials.* **2013**, *34*, 64.
[28] M. K. Jaiswal, J. R. Xavier, J. K. Carrow, P. Desai, D. Alge, A. K. Gaharwar, *ACS Nano.* **2016**, *10*, 246.
[29] A. E. Jakus, A. L. Rutz, S. W. Jordan, A. Kannan, S. M. Mitchell, C. Yun, K. D. Koube, S. C. Yoo, H. E. Whiteley, C. P. Richter, R. D. Galiano, W. K. Hsu, S. R. Stock, E. L. Hsu, R. N. Shah, *Sci. Transl. Med.* **2016**, *8*, 358ra127.
[30] B. Zhang, T. M. Filion, A. B. Kutikov, J. Song, *Adv. Funct. Mater.* **2017**, *27*, 1604784.

[31] C. Ma, X. Tian, J. P. Kim, D. Xie, X. Ao, D. Shan, Q. Lin, M. R. Hudock, X. Bai, J. Yang, *Proceedings of the National Academy of Science of the United States of America*, **2018**, *115*, E11741.
[32] M. Diba, W. A. Camargo, M. Brindisi, K. Farbod, A. Klymov, S. Schmidt, M. J. Harrington, L. Draghi, A. R. Boccaccini, J. A. Jansen, *Adv. Funct. Mater.* **2017**, *27*, 1703438.
[33] E. Lih, C. H. Kum, W. Park, S. Y. Chun, Y. Cho, Y. K. Joung, K. Park, Y. J. Hong, D. J. Ahn, B. Kim, *ACS Nano*. **2018**, *12*, 6917.
[34] M. d'Ischia, A. Napolitano, V. Ball, C. Chen, M. J. Buehler, *Acc. Chem. Res.* **2014**, *47*, 3541.
[35] S. Seo, D. W. Lee, J. S. Ahn, K. Cunha, E. Filippidi, S. W. Ju, E. Shin, B. Kim, Z. A. Levine, R. D. Lins, *Adv. Mater.* **2017**, *29*, 1703026.
[36] Y. Liu, K. Ai, L. Lu, *Chem. Rev.* **2014**, *114*, 5057.
[37] V. K. Thakur, M. Lin, E. J. Tan, P. S. Lee, *J. Mater. Chem.* **2012**, *22*, 5951.
[38] Q. Yu, C. Zhao, Q. Zhu, H. Sui, Y. Yin, J. Li, *Thermochim. Acta* **2020**, *686*, 178530.
[39] S. J. Park, J. Lee, J. W. Choi, J. H. Yang, J. H. Lee, J. Lee, Y. Son, C. W. Ha, N. Lee, S. H. Kim, *Mater. Sci. Eng., C* **2021**, *118*, 111406.
[40] C. A. Silvera Batista, R. G. Larson, N. A. Kotov, *Science* **2015**, *350*, 1242477.
[41] Y. Huang, L. Chen, S. Zheng, X. Wu, L. Liu, K. Zhang, K. Ke, Z. Liu, W. Yang, M. Yang, *Adv. Mater. Technol.* **2021**, *6*, 2001084.
[42] M. Tlotleng, E. Akinlabi, M. Shukla, S. Pityana, *Mater. Sci. Eng., C* **2014**, *43*, 189.
[43] K. Oh, K. Lee, J. Choi, *Mater. Lett.* **2017**, *192*, 137.
[44] H. Jung, T. Jang, L. Wang, H. Kim, Y. Koh, J. Song, *Biomaterials.* **2015**, *37*, 49.
[45] T. Jang, J. H. Lee, S. Kim, C. Park, J. Song, H. J. Jae, H. Kim, J. W. Chung, H. Jung, *Biomaterials* **2019**, *223*, 119461.
[46] K. Cheon, C. Park, M. Kang, I. Kang, M. Lee, H. Lee, H. Kim, H. Jung, T. Jang, *Bioactive Materials* **2021**, *6*, 1189.
[47] S. R. Paital, N. B. Dahotre, *Materials Science and Engineering: R: Reports* **2009**, *66*, 1.
[48] S. Chen, Q. Shi, T. Jang, M. S. B. Ibrahim, J. Deng, G. Ferracci, W. S. Tan, N. Cho, J. Song, *Adv. Funct. Mater.* **2021**, *31*, 2106276.
[49] H. B. Lee, Y. W. Kim, S. H. Kim, S. H. Park, J. Choi, C. AranasJr, *Small.* **2018**, *14*, 1801349.
[50] S. H. Kim, S. Yeon, J. H. Lee, Y. W. Kim, H. Lee, J. Park, N. Lee, J. P. Choi, C. AranasJr, Y. J. Lee, *Virtual and Physical Prototyping.* **2020**, *15*, 460.
[51] S. H. Kim, S. Yeon, J. H. Kim, S. J. Park, J. E. Lee, S. Park, J. Choi, C. AranasJr, Y. Son, *ACS Appl. Mater. Interfaces* **2019**, *11*, 17090.
[52] M. Lee, H. Lee, C. Park, I. Kang, J. Kim, H. Kim, H. Jung, T. Jang, *Bioactive Materials* **2022**, *9*, 239.